Monthly Notices of the ROYAL ASTRONOMICAL SOCIETY

MNRAS **531,** 1149–1157 (2024) https://doi.org/10.1093/mnras/stae1208
Advance Access publication 2024 May 07

Discovery of evolving low-frequency QPOs in hard X-rays (∼100 keV) observed in black hole Swift J1727.8−1613 with *AstroSat*

Anuj Nandi,[1]★ Santabrata Das,[2]★ Seshadri Majumder,[2] Tilak Katoch,[3] H. M. Antia[4] and Parag Shah[3]

[1]*Space Astronomy Group, ISITE Campus, U. R. Rao Satellite Centre, Outer Ring Road, Marathahalli, Bangalore 560037, India*
[2]*Department of Physics, Indian Institute of Technology Guwahati, Guwahati 781039, India*
[3]*DAA, Tata Institute of Fundamental Research, Colaba, Mumbai 400005, India*
[4]*UM-DAE Centre for Excellence in Basic Sciences, University of Mumbai, Kalina, Mumbai 400098, India*

Accepted 2024 April 24. Received 2024 March 23; in original form 2023 November 17

ABSTRACT

We report the first detection of evolving low-frequency quasi-periodic oscillation (LFQPO) frequencies in hard X-rays upto 100 keV with *AstroSat*/LAXPC during 'unusual' outburst phase of Swift J1727.8−1613 in hard intermediate state (HIMS). The observed LFQPO in 20–100 keV has a centroid $\nu_{\rm QPO} = 1.43$ Hz, a coherence factor $Q = 7.14$ and an amplitude $\rm rms_{QPO} = 10.95$ per cent with significance $\sigma = 5.46$. Type-C QPOs (1.09–2.6 Hz) are found to evolve monotonically during HIMS of the outburst with clear detection in hard X-rays (80−100 keV), where $\rm rms_{QPO}$ decreases (∼ 12–3 per cent) with energy. Further, $\nu_{\rm QPO}$ is seen to correlate (anticorrelate) with low- (high-) energy flux in 2–20 keV (15–50 keV). Wide-band (0.7−40 keV) energy spectrum of *NICER*/XTI and *AstroSat*/LAXPC is satisfactorily described by the 'dominant' thermal Comptonization contribution (∼88 per cent) in presence of a 'weak' signature of disc emissions ($kT_{\rm in} \sim 0.36$ keV) indicating the harder spectral distribution. Considering source mass $M_{\rm BH} = 10\,{\rm M}_{\odot}$ and distance $1.5 < {\rm d\ (kpc)} < 5$, the unabsorbed bolometric luminosity is estimated as ∼ 0.03–0.92 per cent $L_{\rm Edd}$. Finally, we discuss the implications of our findings in the context of accretion dynamics around black hole X-ray binaries.

Key words: accretion, accretion discs – black hole physics – radiation mechanisms: general – stars: individual: Swift J1727.8−1613 – X-rays: binaries.

1 INTRODUCTION

Black hole X-ray binaries (BH-XRBs) are the ideal cosmic laboratories to understand the underlying physical mechanisms that govern the accretion dynamics around the compact objects. Interestingly, the accreting systems become more complex when BH-XRBs undergo various spectral state transitions during the outburst phases (and references therein Belloni et al. 2005; Remillard & McClintock 2006; Nandi et al. 2012; Iyer, Nandi & Mandal 2015; Sreehari et al. 2019; Baby et al. 2021; Prabhakar et al. 2023). Indeed, these sources often exhibit low-frequency quasi-periodic oscillation (LFQPO) features (0.1 to ≲30 Hz) in the power spectra (Remillard & McClintock 2006), which generally evolve during the onset phase of the outburst. In general, LFQPOs are considered as an effective diagnostic tool to examine the accretion scenarios (Chakrabarti & Manickam 2000; Chakrabarti et al. 2008; Nandi et al. 2012; Iyer et al. 2015) and the nature of the central source (Motta et al. 2014a, b). Usually, LFQPO features are observed at low energies (≲40 keV) (and references therein Sreehari et al. 2019; Aneesha et al. 2023) except for very few sources (i.e. GRS 1915+105, Tomsick & Kaaret 2001; MAXI J1535−571, Huang et al. 2018; MAXI J1820+070, Ma et al. 2021; MAXI J1803−298, Wang et al. 2021; MAXI J1631−479, Bu et al. 2021), where LFQPOs are observed at higher energies. Needless to mention that the detection of LFQPO signatures at higher energies is a rare phenomenon and its origin remains unclear till date.

Keeping this in mind, we examine the LFQPO features in hard X-rays observed with *AstroSat* for a X-ray transient source Swift J1727.8−1613 recently discovered by *Swift*/BAT on 2023 August 24 (Kennea & Swift Team 2023; Negoro et al. 2023). Immediate monitoring of the source with Monitor of All-sky X-ray Image/Gas Slit Camera (MAXI/GSC) in 2–20 keV reveals an 'unusual' peak in its X-ray flux from 150 mCrab to 3 Crab within a day (Nakajima et al. 2023) that ultimately reaches to peak value ∼7 Crab. Meanwhile, the radio counterpart of the source appears to be consistent with its optical position, and Very Large Array (VLA; 5.25 GHz) and Allen Telescope Array [(ATA; 5 GHz)] independently observe an increase of radio flux from ∼18 to 107 mJy (Bright et al. 2023; Miller-Jones et al. 2023) just after 6 d of the source discovery. Further, VLA Low-band Ionosphere and Transient Experiment (VLITE) continuously monitor the source in the radio frequency at 338 MHz (Peters et al. 2023). Interestingly, during the fast rising period of the ongoing outburst, strong QPOs in the frequency range 0.44–0.88 Hz are observed by both *NICER* and *Swift*/BAT (Draghis et al. 2023; Palmer & Parsotan 2023). *AstroSat* also observed this source on 2023 September 2 and a prominent QPO signature was detected in the power spectra at 1.1 Hz along with harmonic at 2.0 Hz (Katoch et al. 2023). In addition, Imaging X-ray Polarimetry

★ E-mail: anuj@ursc.gov.in (AN); sbdas@iitg.ac.in (SD)

Explorer (*IXPE*) reported the detection of polarized emission in hard intermediate state (HIMS) of the source with polarization degree PD $\sim$ 4.1 per cent $\pm$ 0.2 per cent and polarization angle PA $\sim$ 2.2° $\pm$ 1.3°. Based on the polarization results and comparing X-ray flux with known BH-XRBs, the inclination and distance of the source are predicted as $i \sim 30°$–$60°$ and 1.5 kpc (Veledina et al. 2023), respectively.

In this paper, for the first time to the best of our knowledge, we report the detection of energy resolved LFQPO at frequencies $\nu_{\rm QPO} \sim 1.4$–2.6 Hz in hard X-rays ($\sim$100 keV) during HIMS of Swift J1727.8−1613. Needless to mention that the large effective area of *AstroSat*/Large Area X-ray Proportional Counter (LAXPC) makes it possible to study the variability of LFQPO at high energies. We also present the systematic evolution of LFQPO frequencies using *AstroSat* observations (augmented with *NICER* and *Swift* detections) during the onset phase of the outburst. The hardness–intensity variation along with the spectral study suggests that the source evolved from Low Hard State (LHS) to High Soft State (HSS) via intermediate states [HIMS and Soft Intermediate State (SIMS)]. At present, the source transits through the decay phase.

This paper is organized as follows. In Section 2, we mention observation details and data analysis procedures for each instruments. In Section 3, we present results associated with source outburst, detection, and evolution of LFQPO at hard X-rays including spectral modelling. Finally, in Section 4, we conclude with discussion.

2 OBSERVATION AND DATA REDUCTION

AstroSat (Agrawal et al. 2017) observed Swift J1727.8−1613 on 2023 September 2 (MJD 60189) for the first time during a slew mode operation with an offset of $\sim$0.9° from the pointing (RA = 261.13°, Dec. = −16.01°) for 11 s ($T_{\rm start}$ = 14:18 UT) exposure only. The source was further observed by *AstroSat* as a part of Target of Opportunity (ToO)[1] campaign during 2023 September 08 (MJD 60195) to 2023 September 14 (MJD 60201) for a total exposure of $\sim$207 ks. During slew mode, LAXPC20 was operational although it was switched off during ToO observations for safety reasons to avoid detector saturation due to very high source count rates. LAXPC10 was operational in a low gain mode for ToO observations. Note that we use LAXPC10 data for temporal analysis only, where data were collected in event mode (EA).

LAXPC level-1 data are processed by LAXPCSOFT V3.4.4[2] to extract events, light curves, spectra, and background files for the good time intervals (GTIs). The LAXPC background is estimated from the blank sky observations (Antia et al. 2017, 2021, 2022) made close to the source observation. While using data from slew mode operation, we use the off-axis response matrix file for LAXPC20 (LX20CSHM13OFF50 V1.0.RMF) for channel to energy conversion to carry out both timing and spectral analyses (Antia et al. 2017; Baby et al. 2021; Katoch et al. 2021; Bhuvana et al. 2023). As LAXPC10 operates at low gain mode, the channel to energy mapping remains uncertain. Hence, we obtain energy-channel relation using the 60 keV calibration peak in the veto anode A8 (Antia et al. 2017) and a feature in background spectrum (observed before ToO observation) around 30 keV. These peaks were attributed around channels 70 and 35, respectively, in 1024 channel space of LAXPC10, suggesting an approximately linear response. Employing this scaling, we estimate the low-energy threshold to be around 20 keV. With this, we adopt a linear relation to obtain energy-resolved light curve. Light curves are generated using single event, all layers data of LAXPC10 (Sreehari et al. 2020; Katoch et al. 2021).

Swift J1727.8−1613 is also observed with *NICER* almost on a daily basis since its discovery. In this work, we analyse the *NICER* observations on 2023 September 2, 8, and 13, quasi-simultaneous with *AstroSat* observations. Two more observations on 2023 August 25 and October 2 in different phases of the outburst are also analysed. The data are processed using the *NICER* data analysis software (NICERDAS V10) available in HEASOFT V 6.32.1[3] with the appropriate calibration data base. The task NICER12 is used to generate clean event files considering all the standard calibration and data screening criteria. Further, the spectral products are extracted employing `nicerl3-spect` tool. We select the background model `3c50` using the flag `bkgmodeltype = 3c50` during the extraction of spectral products.

3 MODELLING AND RESULTS

3.1 Outburst profile and hardness–intensity diagram

We study the outburst profile of Swift J1727.8−1613 using data from multiple instruments (MAXI, BAT, and VLITE) in different energy bands. Since its detection on 2023 August 24, the source seems to exhibit a canonical outburst profile with a sudden rise from quiescence followed by a slow decay. In Figs 1(a–c), we present the results obtained from (a) 0.2 d averaged monitoring with MAXI/GSC (2–20 keV), (b) 1 d binned light curve from *Swift*/BAT (15–50 keV), and (c) radio detections using VLITE (at 338 MHz), respectively. During the initial phase of the outburst ($\sim$27 d), source is observed with 'compact' radio emission of flux $\sim$80 mJy. However, a significant increase of radio emission $\sim$150 mJy is observed during the transition from HIMS to SIMS, which is followed by strong radio flare with flux $\sim$350 mJy after $\sim$15 d (Peters et al. 2023). In panel (d), we depict the variation of hardness ratio (HR) defined as the ratio of photon counts in 6–20 to 2–6 keV energy bands of MAXI/GSC. We show the evolution of detected Type-C QPO frequency ($\nu_{\rm QPO}$) during the onset phase of outburst observed with *NICER*, *Swift*, and *AstroSat* in panel (e).

In Fig. 1(f), we present the hardness–intensity diagram (HID) obtained from the MAXI/GSC monitoring, where the variation of intensity (photons cm^{-2} s^{-1}) in 2–20 keV energy range is plotted with HR. The obtained results are plotted using colour-coded filled circles where colourbar indicates the day number since the discovery of the source (see also panels Figs 1a–d). As the outburst progresses, the source traces different spectral states, namely LHS with HR $\sim$0.6–0.47 (D0–D3), HIMS with HR $\sim$0.47–0.19 (D3−D27), SIMS(R) with HR $\sim$0.19–0.02 (D27−D80), a long-lived HSS with HR $\lesssim$0.02 (D80−D130), respectively. At present, the source probably evolves through the decay phase of SIMS (D130−till date) with HR $\gtrsim$0.02 and flux lavel $\sim$70 mCrab of the ongoing outburst. Note that the observed radio detection which is strongly correlated with the spectral states, further confirms the transition from HIMS to SIMS ($\sim$D27) of the source along with strong radio flare detected during SIMS.

[1] https://astrobrowse.issdc.gov.in/astro_archive/archive/Home.jsp
[2] https://www.tifr.res.in/~astrosat_laxpc/LaxpcSoft.html
[3] https://heasarc.gsfc.nasa.gov/docs/software/heasoft/

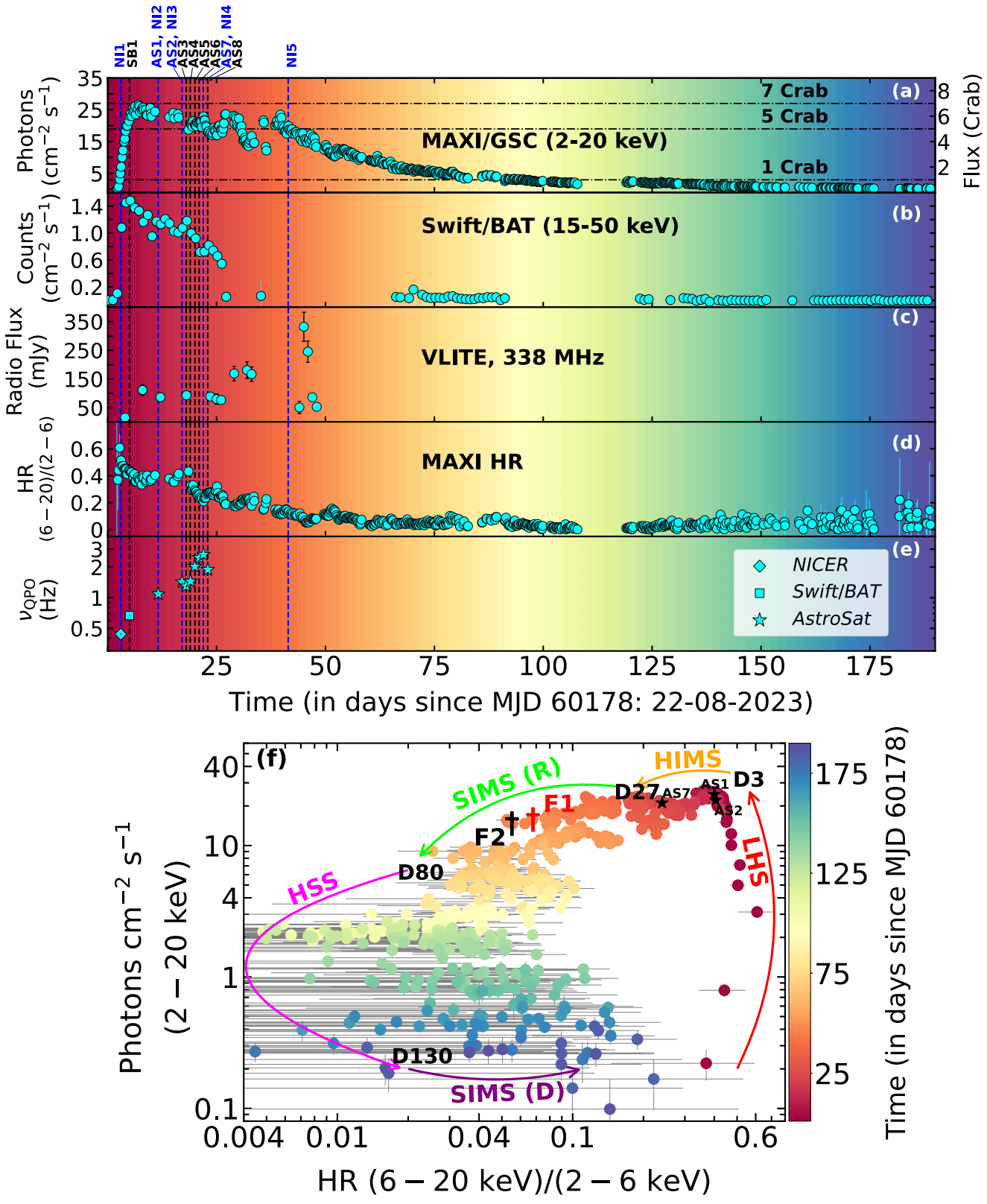

Figure 1. Long term monitoring of Swift J1727.8−1613 with multiple instruments in different energy bands. In panels (a) and (b), variation of MAXI/GSC and *Swift*/BAT count rates in 2–20 and 15–50 keV energy ranges are shown. Panel (c) represents radio flux with VLITE at 338 MHz. Variation of hardness ratio obtained from MAXI/GSC is plotted in panel (d). Evolution of ν_{QPO} in Swift J1727.8−1613 detected from different instruments is shown in panel (e). Hardness–intensity diagram obtained from MAXI/GSC observations in 2–20 keV energy band is shown in panel (f). Colourbar indicates day number since source discovery.

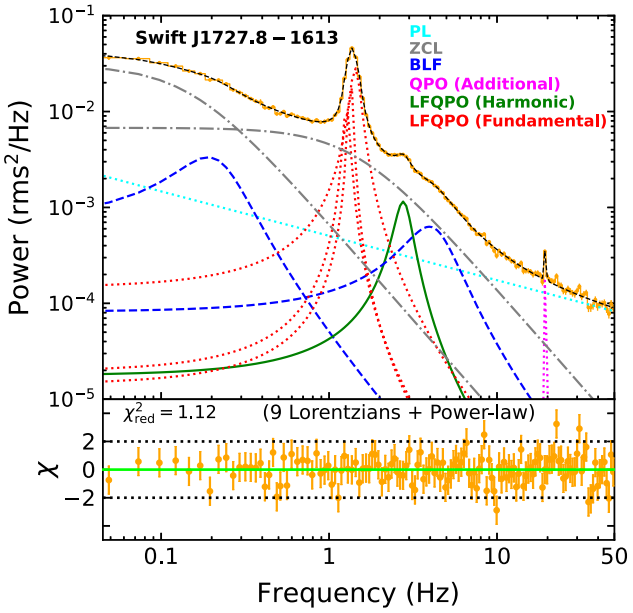

Figure 2. Best-fitting PDS of AS2 observation (MJD 60195) of Swift J1727.8−1613 in 20–100 keV energy band. The different model components (nine `Lorentzian` and one `power-law`) corresponding to different characteristics are used to fit the entire PDS. The variation of residuals is shown in the bottom panel. See the text for details.

3.2 Detection and evolution of LFQPO in hard X-rays

We examine the power density spectra (PDS) using the archival LAXPC10 data during the outburst phase (see Section 2, Figs 1a–b). While doing so, 0.01 s time binned light curves in 20–100 keV energy range are used to generate PDS up to the Nyquist frequency (50 Hz) using ftool `powspec`[4] within HEASOFT v6.32.1.[5] We choose 4096 newbins per interval that results 2048 frequency points in the unbinned PDS. These 2048 frequency points are further geometrically rebinned with a factor of 1.03 to obtain the resultant PDS with 140 frequency bins in unit of rms^2 Hz^{-1} (Sreehari et al. 2019). Accordingly, each frequency bin contains ∼15 data points which are averaged out. Because of this, the underlying likelihood function tends to follow a Gaussian distribution (van der Klis 1989; Vaughan 2010) in accordance with the central limit theorem and therefore, the chi-square statistics remain valid for PDS modelling (Papadakis & Lawrence 1993).

Each PDS is modelled with a combination of multiple `Lorentzian` (van der Klis 1994b, a; Nowak 2000; Belloni, Psaltis & van der Klis 2002; Belloni et al. 2005; Kushwaha, Agrawal & Nandi 2021) and a `power-law` component within XSPEC environment. A `Lorentzian` is characterized by three parameters: centroid (LC), width (LW), and normalization (LN). In Fig. 2, we present the various model components to describe the PDS continuum and QPO features of epoch AS2 (MJD 60195) in 20–100 keV energy range. While doing so, we use two zero-centred `Lorentzian` (ZCL; dot–dashed in grey), two bump-like features (BLF; dashed in blue) at ∼0.2 and ∼4 Hz, and one power-law component (PL; dotted in cyan) to model the entire continuum in 0.1–50 Hz frequency range. In addition, in modelling the complex nature of LFQPO feature (see also Dotani et al. 1989; Belloni et al. 2002), we use three `Lorentzian` (dotted in red) at three distinct nearby frequencies of ∼1.27, ∼1.34, and ∼1.43 Hz. Further, one additional `Lorentzian` (solid in green) profile is required to model the harmonic feature at ∼2.76 Hz. Finally, one more `Lorentzian` (dotted in magenta) is needed to model a possible QPO-like feature at ∼20 Hz. With this, we obtain best-fitting PDS with a χ^2_{red} ($\chi^2/d.o.f$) of 131/117 = 1.12 that yields a strong LFQPO feature of frequency $\nu_{QPO} \sim 1.43$ Hz in 20–100 keV energy band. We present the best-fitting residuals variation in the bottom panel of Fig. 2. Following the above approach, we further carry out the modelling of the energy dependent PDS of epoch AS2 (MJD 60195). The best-fitting model parameters associated to individual model components used in the PDS fitting are tabulated in Table 1. Similar model combinations are also used to fit the PDS (20–100 keV) of epoch AS7 (MJD 60199) with the exception that the BLFs (∼1, ∼5, and ∼8 Hz) and complex LFQPO features (∼2.17, ∼2.66, and ∼3.29 Hz) are present at different frequencies.

We verify the significance of the LFQPO features by comparing the chi-square statistics obtained from the best-fitting due to the inclusion of respective `Lorentzian` components. We also examine χ^2 statistics of the PDS modelling with and without QPO feature. Towards this, we compute the change in fitting chi-square value per degrees of freedom (defined as $\Delta\chi^2_{dof} = (\chi^2_b - \chi^2_a)/\Delta dof$) using best-fitting chi-square value before (χ^2_b) and after (χ^2_a) the inclusion of respective `Lorentzian` component corresponding to the difference in degrees of freedom (Δdof). Accordingly, the best-fitting statistics is realized with the improvement of $\Delta\chi^2_{dof}$ due to the inclusion of respective `Lorentzian` components, which are presented in Table 1. As an example, in 20–100 keV, $\Delta\chi^2_{dof}$ are computed due to the difference of best-fitting PDS for L1–L8 and L1–L9 components, which renders $\Delta\chi^2_{dof} = 309/3 = 103$. Similar approach is followed in determining the chi-square statistics for other energy bands. The estimated $\Delta\chi^2_{dof}$ due to the inclusion of respective `Lorentzian` components are presented in Table 1 for all PDS of AS2. Needless to mention that the requirement of the different model components to obtain the best-fitting PDS is clearly justified as $\Delta\chi^2_{dof}$ improves significantly. We continue to carry out the analyses for AS7 as well, however we refrain in presenting it to avoid repetition.

Following the standard approach (and references therein Belloni & Altamirano 2013; Sreehari et al. 2019; Majumder et al. 2022, 2023), we estimate the *significance* ($\sigma = LN/\mathrm{err}_{neg}$), and *Q factor* ($\equiv \nu_{QPO}/\Delta\nu$) for QPO features. We obtain σ and *Q factor* for fundamental LFQPO as 5.46σ (22.97σ) and 7.14 (5.02) for epoch AS2 (AS7), respectively. We further estimate the percentage rms amplitude (rms_{QPO}; Ribeiro et al. 2019; Sreehari et al. 2020) of the detected LFQPO and obtained as 10.95 per cent (9.21 per cent) for epoch AS2 (AS7). Note that in both AS2 and AS7 epochs, we consider the centroid frequency of LFQPO that renders maximum power. Subsequently, the LFQPO parameters are computed for this component only. All the best-fitting models and estimated parameters are tabulated in Table 2. In Fig. 1(e), we present the evolution of ν_{QPO} (1.09–2.66 Hz) during the entire *AstroSat* campaign along with *NICER* and *Swift*/BAT detection in 0.44–0.8 Hz frequency range.

We further study the energy dependent properties of the detected LFQPO features. Towards this, we generate PDS in different energy bands, namely 20–40, 40–60, 60–80, and 80–100 keV. We detect strong Type-C LFQPO features in all the aforementioned energy bands (see Table 2) and observe that the centroid frequency (ν_{QPO}) remains independent of X-ray photon energy as shown in Fig. 3 (AS2 and AS7 epochs). It may be noted that a ZCL component along with an additional `Lorentzian` at ν_{QPO} are used to fit the PDS in higher energy band (80–100 keV). In order to confirm the detection

[4]https://heasarc.gsfc.nasa.gov/xanadu/xronos/examples/powspec.html
[5]https://heasarc.gsfc.nasa.gov/lheasoft/release_notes.html

Table 1. All the model parameters obtained from the best-fitting PDS of epoch AS2 (MJD 60195) in different energy bands. Here, α_{PL}, $norm_{PL}$, and $L_i (i = 1, 2, 3, 4, 5, 6, 7, 8, 9)$ represent the power-law index, normalization, and `Lorentzian` components used in the fitting, respectively. LC, LW, and LN are the `Lorentzian` centroid frequency, FWHM, and normalization, respectively. A `constant` component (instead of `power-law`) is used for the modelling of 60–80 and 80–100 keV energy band PDS. $\Delta\chi^2_{dof}$ represents the improvement in χ^2 per d.o.f. due to the inclusion of respective model components. Parameters in bold font indicate the fundamental QPO components. See the text for details.

	PL			ZCL		BLF		QPO (Additional)	LFQPO (Harmonic)	LFQPO (Fundamental)			
Energy (keV)	α_{PL}	$norm_{PL}$ ($\times 10^{-4}$)		L_1	L_2	L_3	L_4	L_5	L_6	L_7	L_8	L_9	$\chi^2/d.o.f$
			$\Delta\chi^2_{dof}$	30	18	62	4	46	41	18	12	103	
20−100	$0.46^{+0.08}_{-0.09}$	$5.05^{+1.02}_{-0.89}$	LC	0.0	0.0	$3.94^{+0.13}_{-0.15}$	$0.19^{+0.04}_{-0.05}$	$19.46^{+0.02}_{-0.06}$	$2.76^{+0.02}_{-0.02}$	$1.27^{+0.01}_{-0.01}$	$1.34^{+0.01}_{-0.01}$	$\mathbf{1.43^{+0.02}_{-0.02}}$	131/117
			LW	$2.88^{+0.37}_{-0.38}$	$0.30^{+0.05}_{-0.05}$	$3.05^{+0.31}_{-0.30}$	0.2[a]	0.1[a]	$0.69^{+0.09}_{-0.09}$	0.1[a]	0.06[a]	$\mathbf{0.20^{+0.03}_{-0.01}}$	
			LN	$0.015^{+0.002}_{-0.002}$	$0.007^{+0.001}_{-0.001}$	$0.0027^{+0.0005}_{-0.0004}$	$0.0009^{+0.0004}_{-0.0003}$	$0.00013^{+0.00001}_{-0.00001}$	$0.0012^{+0.0002}_{-0.0002}$	$0.0019^{+0.0003}_{-0.0003}$	$0.0027^{+0.0006}_{-0.0006}$	$\mathbf{0.00915^{+0.00071}_{-0.00169}}$	
			$\Delta\chi^2_{dof}$	54	56	42	3	29	41	43	20	158	
20−40	$0.31^{+0.04}_{-0.05}$	$5.00^{+0.85}_{-0.75}$	LC	0.0	0.0	$3.94^{+0.13}_{-0.15}$	$0.22^{+0.02}_{-0.02}$	$19.28^{+0.13}_{-0.12}$	$2.76^{+0.02}_{-0.02}$	$1.27^{+0.01}_{-0.01}$	$1.38^{+0.01}_{-0.02}$	$\mathbf{1.42^{+0.02}_{-0.02}}$	
			LW	$2.82^{+0.24}_{-0.25}$	$0.32^{+0.02}_{-0.02}$	$3.01^{+0.29}_{-0.28}$	0.1[a]	$0.33^{+0.15}_{-0.16}$	$0.72^{+0.11}_{-0.09}$	0.07[a]	0.1[a]	$\mathbf{0.22^{+0.02}_{-0.02}}$	128/116
			LN	$0.019^{+0.001}_{-0.001}$	$0.0097^{+0.0006}_{-0.0006}$	$0.0035^{+0.0007}_{-0.0006}$	$0.00033^{+0.00016}_{-0.00015}$	$0.00015^{+0.00003}_{-0.00003}$	$0.0017^{+0.0003}_{-0.0003}$	$0.0028^{+0.0003}_{-0.0006}$	$0.0055^{+0.0009}_{-0.0009}$	$\mathbf{0.00943^{+0.00153}_{-0.00145}}$	
			$\Delta\chi^2_{dof}$	105	–	60	9	–	–	–	–	457[b]	
40−60	$0.21^{+0.04}_{-0.04}$	$17.61^{+2.29}_{-2.23}$	LC	0.0	–	$2.87^{+0.10}_{-0.13}$	$0.72^{+0.03}_{-0.03}$	–	–	–	–	$\mathbf{1.38^{+0.01}_{-0.01}}$	
			LW	$0.45^{+0.02}_{-0.02}$	–	$2.76^{+0.52}_{-0.43}$	$0.28^{+0.17}_{-0.12}$	–	–	–	–	$\mathbf{0.23^{+0.02}_{-0.02}}$	135/127
			LN	$0.013^{+0.001}_{-0.001}$	–	$0.007^{+0.001}_{-0.001}$	$0.0009^{+0.0004}_{-0.0003}$	–	–	–	–	$\mathbf{0.01291^{+0.00064}_{-0.00056}}$	
		`constant` ($\times 10^{-4}$)	$\Delta\chi^2_{dof}$	87	–	9	–	16	–	–	–	38	
60−80	–	$12.02^{+0.22}_{-0.24}$	LC	0.0	–	$1.51^{+0.81}_{-0.79}$	–	$19.34^{+0.15}_{-0.22}$	–	–	–	$\mathbf{1.37^{+0.01}_{-0.01}}$	
			LW	$0.43^{+0.06}_{-0.06}$	–	$4.18^{+2.68}_{-1.27}$	–	0.1[a]	–	–	–	$\mathbf{0.24^{+0.04}_{-0.04}}$	153/129
			LN	$0.0036^{+0.0004}_{-0.0005}$	–	$0.0033^{+0.0013}_{-0.0012}$	–	$0.0007^{+0.0001}_{-0.0001}$	–	–	–	$\mathbf{0.00243^{+0.00040}_{-0.00031}}$	
			$\Delta\chi^2_{dof}$	10	–	–	–	–	–	–	–	3	
80−100	–	$16.31^{+0.26}_{-0.26}$	LC	0.0	–	–	–	–	–	–	–	$\mathbf{1.37^{+0.04}_{-0.05}}$	
			LW	$0.61^{+0.39}_{-0.22}$	–	–	–	–	–	–	–	$\mathbf{0.17^{+0.13}_{-0.07}}$	77/91
			LN	$0.00104^{+0.00031}_{-0.00026}$	–	–	–	–	–	–	–	$\mathbf{0.00042^{+0.00014}_{-0.00013}}$	

Notes. [a]Frozen at best-fitting values as errors are not constrained.

[b]Higher $\Delta\chi^2_{dof}$ signifies very strong fundamental LFQPO (L9 component) in the absence of L7 and L8 components.

Table 2. Best-fitting QPO and harmonic characteristics obtained from different observations with LAXPC20 (AS1) and LAXPC10 (AS2 and AS7) of *AstroSat*. All the quantities mentioned in the table have their usual meanings. See the text for details.

		Fundamental QPO characteristics					Harmonic characteristics						
Epoch (Date)	Energy Range	ν_{QPO} (Hz)	$\Delta\nu$ (Hz)	Q *factor*	Sig. ($\sigma = \frac{LN}{err_{neg}}$ [a])	rms_{QPO} (per cent)	ν_{har} (Hz)	$\Delta\nu$ (Hz)	Q *factor*	Sig. ($\sigma = \frac{LN}{err_{neg}}$ [a])	rms_{har} (per cent)	rms_{tot} (per cent)	χ^2_{red} ($\chi^2/d.o.f$)
AS1	3−100	$1.09^{+0.02}_{-0.02}$	$0.05^{+0.03}_{-0.04}$	21.80	2.20	9.84 ± 5.84	$2.16^{+0.25}_{-0.11}$	$0.79^{+0.56}_{-0.27}$	2.73	3.42	10.02 ± 5.25	22.27 ± 10.39	1.00 (44/44)
(2023-09-02)	3−20	$1.09^{+0.04}_{-0.02}$	$0.05^{+0.02}_{-0.03}$	21.80	2.16	11.42 ± 6.27	$2.24^{+0.34}_{-0.25}$	$0.70^{+0.45}_{-0.32}$	3.20	3.38	10.09 ± 5.05	19.11 ± 11.94	1.02 (45/44)
AS2	20−100	$1.43^{+0.02}_{-0.02}$	$0.20^{+0.03}_{-0.01}$	7.14	5.46	10.95 ± 2.14	$2.76^{+0.04}_{-0.04}$	$0.69^{+0.16}_{-0.14}$	4.00	6.67	6.64 ± 0.31	21.88 ± 1.71	1.12 (131/117)
(2023-09- 08)	20−40	$1.42^{+0.02}_{-0.02}$	$0.22^{+0.02}_{-0.02}$	6.45	6.51	12.62 ± 2.04	$2.76^{+0.03}_{-0.04}$	$0.73^{+0.18}_{-0.15}$	3.78	6.37	7.75 ± 0.63	24.82 ± 1.94	1.10 (128/116)
	40−60	$1.38^{+0.01}_{-0.01}$	$0.23^{+0.02}_{-0.02}$	6.00	23.11	10.44 ± 1.28	$3.01^{+0.20}_{-0.25}$	$1.54^{+1.37}_{-0.74}$	1.95	2.47	11.49 ± 2.05	28.65 ± 5.18	1.06 (135/127)
	60−80	$1.37^{+0.01}_{-0.01}$	$0.24^{+0.04}_{-0.04}$	5.71	7.84	5.30 ± 1.22	–	–	–	–	–	26.44 ± 3.06	1.19 (153/129)
	80−100	$1.37^{+0.07}_{-0.07}$	$0.17^{+0.12}_{-0.07}$	8.06	3.23	2.98 ± 1.10	–	–	–	–	–	28.78 ± 3.63	0.85 (77/91)
AS7	20−100	$2.66^{+0.01}_{-0.01}$	$0.53^{+0.03}_{-0.02}$	5.02	22.97	9.21 ± 1.35	–	–	–	–	–	17.55 ± 1.69	1.13 (130/115)
(2023-09-13)	20−40	$2.66^{+0.01}_{-0.01}$	$0.53^{+0.04}_{-0.02}$	5.02	23.90	11.87 ± 2.17	–	–	–	–	–	22.95 ± 0.92	1.37 (157/115)[b]
	40−60	$2.66^{+0.04}_{-0.03}$	$0.63^{+0.12}_{-0.06}$	4.22	11.26	9.57 ± 1.76	–	–	–	–	–	26.46 ± 2.61	1.07 (134/125)
	60−80	$2.69^{+0.06}_{-0.07}$	$0.69^{+0.23}_{-0.18}$	3.90	5.41	5.27 ± 1.24	–	–	–	–	–	24.32 ± 2.98	1.19 (159/134)
	80−100	$2.64^{+0.24}_{-0.08}$	$0.41^{+0.33}_{-0.15}$	6.44	3.81	4.17 ± 1.25	–	–	–	–	–	26.62 ± 3.65	0.88 (80/91)

Notes. [a]err_{neg} being the negative error of normalization of the fitted `Lorentzian`. [b]Higher χ^2_{red} is observed due to the excess residuals at ∼2 and ∼35 Hz (AS7), and we refrain using additional `Lorentzian` for modelling.

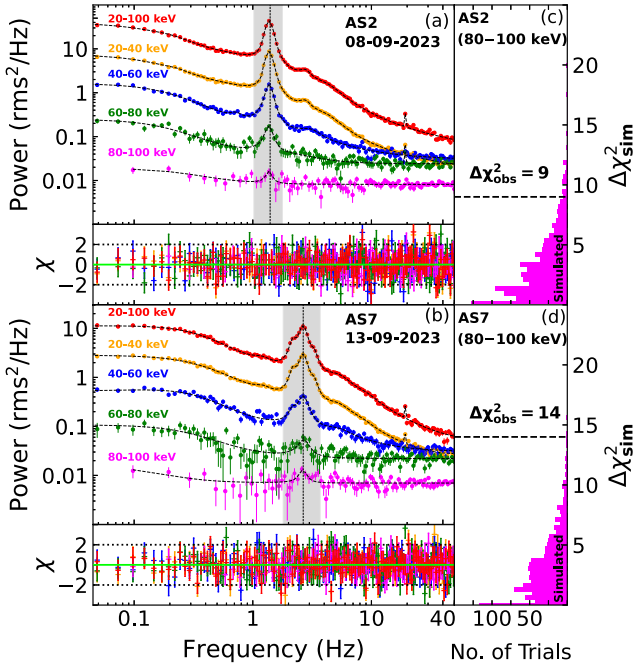

Figure 3. Best-fitting power spectra of Swift J1727.8−1613 in different energy bands (obtained from *AstroSat*/LAXPC10 observations). Panels (a) and (b) are for epoch AS2 and AS7 and residual variations are shown at the bottom of each panel. For clarity, power spectra in 20–100, 20–40, 40–60, 60–80, and 80–100 keV energy bands are scaled by multiplying with constants 950, 150, 40, 20, and 5. Panels (c) and (d) show the results obtained from `simftest` in 80–100 keV energy band of both observations. See the text for details.

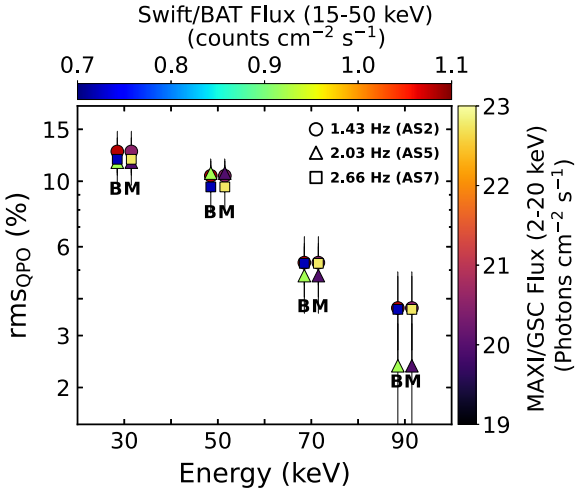

Figure 4. Plot of rms_{QPO} with energy visualized in terms of *Swift*/BAT (B) and MAXI/GSC (M) fluxes. Colour coded filled circles, triangles, and squares denote frequency of LFQPO of ν_{QPO} = 1.43 (AS2), 2.03 (AS5), and 2.66 Hz (AS7), respectively. Points marked with 'B' and 'M' are horizontally shifted for better visibility. Horizontal and vertical colourbars denote *Swift*/BAT and MAXI/GSC fluxes.

significance of QPO, we perform simulation using `simftest` inside XSPEC (Athulya et al. 2022; Bhuvana et al. 2023; Li et al. 2023; Sharma, Jain & Paul 2023) to obtain the probability of best-fitting without the LFQPO features in 80–100 keV energy band. In Figs 3(c–d), we present the distribution of the difference of chi-square values with and without LFQPO feature for 1000 simulated power spectra. The change of the chi-square value obtained from the real observed data ($\Delta\chi^2_{obs}$) by modelling the LFQPO feature is found outside the distribution of the change in chi-square value ($\Delta\chi^2_{sim}$) obtained from the simulation. These findings evidently indicate that the detected ν_{QPO} is directly associated with the hard X-ray emissions. The energy dependent model fitting and estimated parameters along with fit statistics are tabulated in Table 2.

Furthermore, we study the variation of energy-resolved rms amplitude (rms_{QPO}) of the LFQPOs as function of *Swift*/BAT (B) and MAXI/GSC (M) fluxes. The obtained results are shown in Fig. 4, where filled coloured circles, triangles, and squares denote the Type-C LFQPO of ν_{QPO} = 1.43 (AS2), 2.03 (AS5), and 2.66 Hz (AS7) observed with *AstroSat* in different energy bands. In the figure, all points marked with 'B' and 'M' are shifted horizontally for better clarity. The horizontal and vertical colourbars demonstrate the quasi-simultaneous *Swift*/BAT (counts in cm^{-2} s^{-1} within 15–50 keV) and MAXI/GSC (photons in cm^{-2} s^{-1} within 2–20 keV) fluxes. We observe rms_{QPO} ∼ 13 per cent at 20–40 keV which drops

Table 3. Best-fitting and estimated spectral parameters obtained from the fitting of energy spectra with *NICER* and *AstroSat* in 0.6–40 keV energy range. All notations have their usual meanings. The errors are computed with 90 per cent confidence level.

Model components	Model parameters	NI1	AS1 + NI2	NI3	NI4	NI5
		Fitted parameters				
Tbabs	$n_{\rm H}(\times 10^{22})$ cm^{-2}	$0.19^{+0.01}_{-0.01}$	$0.21^{+0.01}_{-0.01}$	$0.20^{+0.01}_{-0.01}$	$0.22^{+0.02}_{-0.01}$	$0.19^{+0.01}_{-0.01}$
diskbb	$kT_{\rm in}$ (keV)	$0.32^{+0.01}_{-0.02}$	$0.36^{+0.01}_{-0.01}$	$0.40^{+0.02}_{-0.02}$	$0.60^{+0.01}_{-0.02}$	$0.70^{+0.01}_{-0.01}$
	$N_{\rm diskbb}(\times 10^5)$	$0.82^{+0.26}_{-0.14}$	$54^{+0.16}_{-0.13}$	$01^{+0.18}_{-0.13}$	$0.13^{+0.02}_{-0.01}$	$0.09^{+0.01}_{-0.01}$
nthcomp	$kT_{\rm e}$ (keV)	$3.93^{+0.69}_{-0.42}$	$6.83^{+0.30}_{-0.29}$	$4.26^{+0.49}_{-0.26}$	4[a]	4.61[a]
	$\Gamma_{\rm nth}$	$60^{+0.01}_{-0.02}$	$84^{+0.01}_{-0.01}$	$80^{+0.02}_{-0.02}$	$96^{+0.01}_{-0.01}$	$2.65^{+0.02}_{-0.02}$
Gaussian	E (keV)	–	$6.41^{+0.06}_{-0.06}$	–	$6.71^{+0.02}_{-0.01}$	–
	σ (keV)	–	0.7[a]	–	$0.30^{+0.13}_{-0.11}$	–
	norm	–	$0.117^{+0.008}_{-0.008}$	–	$0.016^{+0.007}_{-0.006}$	–
		Estimated parameters				
	$F_{\rm disc}$ $(\times 10^{-7})$ erg cm^{-2} s^{-1}	$0.13^{+0.01}_{-0.01}$	$0.35^{+0.01}_{-0.01}$	$0.36^{+0.01}_{-0.01}$	$0.30^{+0.02}_{-0.01}$	$0.37^{+0.01}_{-0.01}$
	$F_{\rm nth}$ $(\times 10^{-7})$ erg cm^{-2} s^{-1}	$27^{+0.02}_{-0.01}$	$3.52^{+0.01}_{-0.01}$	$83^{+0.02}_{-0.02}$	$2.41^{+0.02}_{-0.02}$	$69^{+0.02}_{-0.01}$
	$F_{\rm bol}$ $(\times 10^{-7})$ erg cm^{-2} s^{-1}	$41^{+0.02}_{-0.02}$	$3.98^{+0.01}_{-0.01}$	$2.20^{+0.02}_{-0.01}$	$2.73^{+0.01}_{-0.02}$	$2.06^{+0.03}_{-0.02}$
	Disc contribution (per cent)	9.22	8.79	16.36	10.99	17.96
	Compt. contribution (per cent)	90.07	88.44	83.18	88.24	82.04
	$L_{\rm bol}$ (in $L_{\rm Edd}$)	0.029 ± 0.001[b]	0.082 ± 0.002[b]	0.046 ± 0.001[b]	0.057 ± 0.003[b]	0.042 ± 0.004[b]
		0.32 ± 0.01[c]	0.92 ± 0.01[c]	0.51 ± 0.01[c]	0.63 ± 0.02[c]	0.48 ± 0.04[c]
	τ	12.03 ± 1.20	6.97 ± 0.22	9.49 ± 0.64	8.66 ± 1.88	5.26 ± 1.05
	y- par	4.45 ± 0.21	2.60 ± 0.05	2.99 ± 0.11	2.34 ± 0.15	1.01 ± 0.08
	χ^2/d.o.f ($\chi^2_{\rm red}$)	135/136 (0.99)	223/225 (0.99)	137/135 (1.01)	124/142 (0.87)	159/161 (0.99)

Note. [a]Frozen parameter. [b]Source distance $d = 1.5$ kpc. [c]Source distance $d = 5$ kpc. $L_{\rm Edd} = 1.3 \times 10^{39}$ erg s^{-1} for a 10 $M_\odot$ black hole.

down around ~ 2.5 per cent at 80–100 keV for all epochs under considerations. It is noteworthy that *Swift*/BAT flux anticorrelates with $\nu_{\rm QPO}$ in all energy bands, whereas MAXI/GSC flux increases with $\nu_{\rm QPO}$.

3.3 Spectral energy distribution

We investigate the spectral properties of Swift J1727.8−1613 using combined *NICER*/XTI and *AstroSat*/LAXPC20 observations in 0.6–40 keV energy range. The spectral analysis is carried out for quasi-simultaneous *NICER* and *AstroSat* observations during epoch AS1 and NI2. In addition, the spectral distribution of the source is studied using *NICER* observations NI1, NI3, NI4, and NI5 in 0.6–10 keV energy range, when *AstroSat*/LAXPC20 monitoring were not available.

Spectra are modelled using XSPEC V12.13.0C in HEASOFT V6.31.1. We adopt a model combination `const*Tbabs*(Gaussian + diskbb + smedge*nthcomp)` to describe the spectral distribution. Here, `const` takes care of the cross-calibration between the spectra of different instruments and `Tbabs` is used for the galactic absorption. The models `diskbb` (Makishima et al. 1986) and `nthcomp` (Zdziarski, Johnson & Magdziarz 1996) represent the standard accretion disc and thermal Comptonization components. The `Gaussian` is incorporated in the spectral fitting to model the iron line emission at ∼6.4 keV. Additionally, a `smedge` component is used at ∼9.94 keV to improve the residual variations only for AS1 + NI2 observations. It may be noted that *NICER* spectra showed two instrument lines at 1.8 and 2.2 keV, which are modelled using two additional `Gaussian`. With this, we obtain an acceptable fit with $\chi^2_{\rm red}$ of 0.99. The resultant fit indicates the presence of a weak disc signature having temperature of 0.36 ± 0.01 keV. Moreover, a hard Comptonized spectral tail of photon index 1.84 ± 0.01 and electron temperature $6.83^{+0.30}_{-0.29}$ keV are obtained. We compute the flux associated with different spectral components as well as total bolometric flux using the convolution model `cflux` in 0.5–50 keV energy range. Following Zdziarski et al. (1996) and Majumder et al. (2022), we estimate the optical depth (τ) and Compton y-parameter (y-par). We find that the *NICER* spectra are well-described with the aforementioned model without the `smedge` component. All the model fitted and estimated spectral parameters are tabulated in Table 3. The best-fitting spectra obtained from *NICER* and *AstroSat* observations and the corresponding residuals are shown in Fig. 5.

4 DISCUSSION

In this paper, we report the discovery of evolving LFQPO features (1.4−2.6 Hz) at hard X-rays (∼100 keV) with *AstroSat* during the 'unusual' outburst phase of Swift J1727.8−1613. The source traces the canonical hysteresis loop in the HID with a fugacious HSS followed by a decay phase. During the *AstroSat* campaign, the source was in HIMS dominated by the Comptonized emission (∼ 83–86 per cent) with weak signature of disc emission (∼ 11–16 per cent) and temperature $kT_{\rm in} \sim 0.4$–0.6 keV.

The most fascinating results we report in this work are the significant detection of energy dependent LFQPO features above 40 keV, particularly in the energy range of 80–100 keV with $Q > 6$ and $\sigma > 3$ (see Table 2 and Fig. 3), when the source was in HIMS. We observe that as the outburst progresses, $\nu_{\rm QPO}$ is evolved

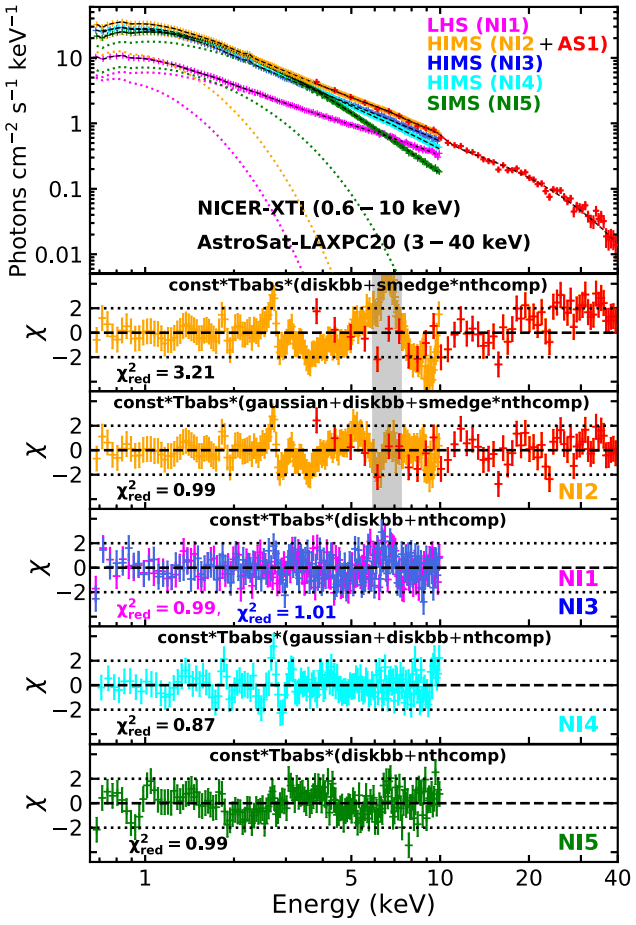

Figure 5. *Upper panel*: Best-fitting energy spectra of Swift J1727.8−1613 with *NICER* and *AstroSat* observations during the onset phase of the outburst. *Lower panels*: Residuals variations obtained from the fitting with different model combinations.

from ∼0.44 to 2.66 Hz during LHS (*NICER* and *Swift*/BAT) and HIMS (*AstroSat*) (see Fig. 1). The unfolded energy spectra (Fig. 5) clearly indicate that the spectral energy distribution is dominated by non-thermal emission with electron temperature $kT_e \sim 4$–7 keV and spectral index $\Gamma \sim 1.6$−1.9 (see Table 2).

The detection of LFQPO ($\nu_{QPO} < 1$ Hz) at high energies (>100 keV) was earlier reported for few BH-XRBs (MAXI J1820+070, Ma et al. 2021 and MAXI J1803−298, Wang et al. 2021), however strong LFQPO ($\nu_{QPO} \sim 1$–10 Hz) at energies <100 keV were observed in MAXI J1535−571 (Huang et al. 2018) and MAXI J1631−479 (Bu et al. 2021) sources. It was suggested that the Lense–Thirring (LT) precession of the inner hot flow can account for the possible origin of Type-C LFQPO of BH-XRBs (see Ingram et al. 2016, for details). Considering this, efforts were further given to investigate the Type-C LFQPOs using LT precession of a small-scale jet, where jet rotates and twists around the spin axis of BH resulting the modulation of the observed flux (Ma et al. 2021). However, this scenario bears limitations as it requires steady increase of jet precession in order to explain the evolution of LFQPO of $\nu_{QPO} \sim 1.09 - 2.66$ Hz as detected in Swift J1727.8−1613 at high energies >40 keV. In addition, while explaining the evolution of ν_{QPO} considering the jet precession model for low-inclination source (∼29°), Bu et al. (2021) claimed that the frequency of Type-C LFQPO generally increases with the decrease of jet height. However, jets are unlikely to be decoupled in LHS/HIMS (Fender, Belloni & Gallo 2004; Fender, Homan & Belloni 2009) and hence, this model also suffers shortcomings to explain the evolution of QPO for Swift J1727.8−1613, although the orbital inclination of this source is recently reported as 40° (Peng et al. 2024). Moreover, as there is no energy dependence of ν_{QPO} observed for this source (see Table 2), it is implausible that any differential precession is involved in exhibiting the LFQPO (Ingram et al. 2016). Needless to mention that the evolution of the Type-C LFQPO ($\nu_{QPO} \sim 0.1$–30 Hz) is observed in the BH-XRBs having time-scale of 5–20 d (Remillard & McClintock 2006; Nandi et al. 2012; Radhika & Nandi 2014; Radhika et al. 2016), which remains challenging to explain till date.

What is more is that the Type-B QPOs are generally observed during the spectral state transition from HIMS to SIMS as well as in SIMS (Fender et al. 2004, 2009; Radhika et al. 2016; Huang et al. 2018; Ingram & Motta 2019, and references therein). However, for Swift J1727.8−1613, we find that all the LFQPOs ($\nu_{QPO} \sim 0.44$–2.66 Hz) are observed in LHS and HIMS with $rms_{QPO} \sim 10$ per cent and $Q > 5$, which are indeed the prime characteristics of a Typc-C QPO (Belloni et al. 2005; Nandi et al. 2012; Ingram & Motta 2019).

Meanwhile, alternate possibilities are also suggested that comprehend the local inhomogeneity in accretion disc yielded the time varying modulation of the inner 'hot' flow and hence, it contributes in resulting ν_{QPO} (Huang et al. 2018; Bu et al. 2021). In reality, this conjecture resembles the corona oscillation scenario caused due to the undulation of the 'hot' and 'dense' downstream flow in the vicinity of the black holes (Molteni, Sponholz & Chakrabarti 1996). Since ν_{QPO} is comparable to the inverse of the infall time-scale (t_{infall}) (Chakrabarti & Manickam 2000) and t_{infall} strongly depends on corona geometry, it is more likely that ν_{QPO} increases as the region occupied by the downstream flow decreases (Chakrabarti et al. 2008; Nandi et al. 2012; Iyer et al. 2015). Indeed, the dynamics of the downstream flow can be regulated by tuning the accretion parameters, namely accretion rate and viscosity (Chakrabarti & Molteni 1993; Das et al. 2014). When the soft photons from the upstream are upscattered at the inner 'hot' flow, high-energy X-ray emissions are produced because of the inverse-Comptonization process (Chakrabarti & Titarchuk 1995; Mandal & Chakrabarti 2005). Accordingly, LFQPO is likely to observe at high energies whenever the source remains in harder spectral state dominated by the Comptonized emission in presence of weak disc signature.

To summarize, we report the first detection of evolving LFQPO features of Swift J1727.8−1613 above 40 keV in HIMS observed with *AstroSat*. In addition, to the best of our knowledge, Swift J1727.8−1613 is the third known BH-XRB that exhibits significant detection of LFQPO (>1 Hz) at higher energies (∼100 keV).

ACKNOWLEDGEMENTS

Authors thank the anonymous reviewer for constructive comments and useful suggestions that help to improve the quality of the manuscript. AN thanks GH, SAG; DD, PDMSA, and Director, URSC for encouragement and continuous support to carry out this research. SD thanks Science and Engineering Research Board (SERB) of India for support under grant MTR/2020/000331. This publication uses the data from the *AstroSat* mission of the Indian Space Research Organisation (ISRO), archived at the Indian Space Science Data Centre (ISSDC). This work has used the data from the LAXPC Instruments developed at TIFR, Mumbai, and the LAXPC-POC at TIFR is thanked for verifying and releasing the data. We also thank the *AstroSat* Science Support Cell hosted by IUCAA and TIFR for providing the LAXPCSOFT software which we used for LAXPC

data analysis. This work has also use data from Monitor of All-sky X-ray Image (MAXI) data provided by Institute of Physical and Chemical Research (RIKEN), Japan Aerospace Exploration Agency (JAXA), and the MAXI team. Also, this research made use of software provided by the High Energy Astrophysics Science Archive Research Center (HEASARC) and NASA's Astrophysics Data System Bibliographic Services. This publication further uses the data from the *NICER* missions, archived at the HEASARC data centre.

DATA AVAILABILITY

Data used for this publication are currently available at the Astrobrowse (*AstroSat* archive) website (https://astrobrowse.issdc.gov.in/astro_archive/archive) of the Indian Space Science Data Center (ISSDC).

REFERENCES

Agrawal P. C. et al., 2017, JAA, 38, 30
Aneesha U., Das S., Katoch T., Nandi A., 2023, in press
Antia H. M. et al., 2017, ApJS, 231, 10
Antia H. M. et al., 2021, JAA, 42, 32
Antia H. M., Agrawal P. C., Katoch T., Manchanda R. K., Mukerjee K., Shah P., 2022, ApJS, 260, 40
Athulya M. P., Radhika D., Agrawal V. K., Ravishankar B. T., Naik S., Mandal S., Nandi A., 2022, MNRAS, 510, 3019
Baby B. E., Bhuvana G. R., Radhika D., Katoch T., Mandal S., Nandi A., 2021, MNRAS, 508, 2447
Belloni T. M., Altamirano D., 2013, MNRAS, 432, 10
Belloni T., Psaltis D., van der Klis M., 2002, ApJ, 572, 392
Belloni T., Homan J., Casella P., van der Klis M., Nespoli E., Lewin W. H. G., Miller J. M., Méndez M., 2005, A&A, 440, 207
Bhuvana G. R., Aneesha U., Radhika D., Agrawal V. K., Mandal S., Katoch T., Nandi A., 2023, MNRAS, 520, 5828
Bright J., Farah W., Fender R., Siemion A., Pollak A., DeBoer D., 2023, Astron. Telegram, 16228, 1
Bu Q. C. et al., 2021, ApJ, 919, 92
Chakrabarti S. K., Manickam S. G., 2000, ApJ, 531, L41
Chakrabarti S. K., Molteni D., 1993, ApJ, 417, 671
Chakrabarti S., Titarchuk L. G., 1995, ApJ, 455, 623
Chakrabarti S. K., Debnath D., Nandi A., Pal P. S., 2008, A&A, 489, L41
Das S., Chattopadhyay I., Nandi A., Molteni D., 2014, MNRAS, 442, 251
Dotani T., Mitsuda K., Makishima K., Jones M. H., 1989, PASJ, 41, 577
Draghis P. A. et al., 2023, Astron. Telegram, 16219, 1
Fender R. P., Belloni T. M., Gallo E., 2004, MNRAS, 355, 1105
Fender R. P., Homan J., Belloni T. M., 2009, MNRAS, 396, 1370
Huang Y. et al., 2018, ApJ, 866, 122
Ingram A. R., Motta S. E., 2019, New A Rev., 85, 101524
Ingram A., van der Klis M., Middleton M., Done C., Altamirano D., Heil L., Uttley P., Axelsson M., 2016, MNRAS, 461, 1967
Iyer N., Nandi A., Mandal S., 2015, ApJ, 807, 108
Katoch T., Baby B. E., Nandi A., Agrawal V. K., Antia H. M., Mukerjee K., 2021, MNRAS, 501, 6123
Katoch T., Antia H. M., Nandi A., Shah P., 2023, Astron. Telegram, 16235, 1
Kennea J. A., Swift Team, 2023, GCN, 34540, 1
Kushwaha A., Agrawal V. K., Nandi A., 2021, MNRAS, 507, 2602
Li P. P. et al., 2023, MNRAS, 525, 595
Ma X. et al., 2021, Nat. Astron., 5, 94
Majumder S., Sreehari H., Aftab N., Katoch T., Das S., Nandi A., 2022, MNRAS, 512, 2508
Majumder S., Das S., Agrawal V. K., Nandi A., 2023, MNRAS, 526, 2086
Makishima K., Maejima Y., Mitsuda K., Bradt H. V., Remillard R. A., Tuohy I. R., Hoshi R., Nakagawa M., 1986, ApJ, 308, 635
Mandal S., Chakrabarti S. K., 2005, A&A, 434, 839
Miller-Jones J. C. A., Sivakoff G. R., Bahramian A., Russell T. D., 2023, Astron. Telegram, 16211, 1
Molteni D., Sponholz H., Chakrabarti S. K., 1996, ApJ, 457, 805
Motta S. E., Belloni T. M., Stella L., Muñoz-Darias T., Fender R., 2014a, MNRAS, 437, 2554
Motta S. E., Munoz-Darias T., Sanna A., Fender R., Belloni T., Stella L., 2014b, MNRAS, 439, L65
Nakajima M. et al., 2023, Astron. Telegram, 16206, 1
Nandi A., Debnath D., Mandal S., Chakrabarti S. K., 2012, A&A, 542, A56
Negoro H. et al., 2023, Astron. Telegram, 16205, 1
Nowak M. A., 2000, MNRAS, 318, 361
Palmer D. M., Parsotan T. M., 2023, Astron. Telegram, 16215, 1
Papadakis I. E., Lawrence A., 1993, MNRAS, 261, 612
Peng J.-Q. et al., 2024, ApJ, 960, L17
Peters W. M., Polisensky E., Clarke T. E., Giacintucci S., Kassim N. E., 2023, Astron. Telegram, 16279, 1
Prabhakar G., Mandal S., Bhuvana G. R., Nandi A., 2023, MNRAS, 520, 4889
Radhika D., Nandi A., 2014, Adv. Space Res., 54, 1678
Radhika D., Nandi A., Agrawal V. K., Seetha S., 2016, MNRAS, 460, 4403
Remillard R. A., McClintock J. E., 2006, ARA&A, 44, 49
Ribeiro E. M., Méndez M., de Avellar M. G. B., Zhang G., Karpouzas K., 2019, MNRAS, 489, 4980
Sharma R., Jain C., Paul B., 2023, MNRAS, 526, L35
Sreehari H., Ravishankar B. T., Iyer N., Agrawal V. K., Katoch T. B., Mandal S., Nandi A., 2019, MNRAS, 487, 928
Sreehari H., Nandi A., Das S., Agrawal V. K., Mandal S., Ramadevi M. C., Katoch T., 2020, MNRAS, 499, 5891
Tomsick J. A., Kaaret P., 2001, ApJ, 548, 401
van der Klis M., 1989, in Ögelman H., van den Heuvel E. P. J., eds, NATO ASI Ser. C Vol. 262, Timing Neutron Stars. Kluwer Academic/Plenum Publishers, New York, p.27
van der Klis M., 1994a, ApJS, 92, 511
van der Klis M., 1994b, A&A, 283, 469
Vaughan S., 2010, MNRAS, 402, 307
Veledina A. et al., 2023, ApJ, 958, L16
Wang Y. et al., 2021, Astron. Telegram, 14613, 1
Zdziarski A. A., Johnson W. N., Magdziarz P., 1996, MNRAS, 283, 193

This paper has been typeset from a TEX/LATEX file prepared by the author.